Article

Theoretical Studies on the Photophysical Properties of the Ag(I) Complex for Thermally Activated Delayed Fluorescence Based on TD-DFT and Path Integral Dynamic Approaches

LingLing Lv,* Kun Yuan, TianYu Zhao, HuiXue Li, and YongCheng Wang

Read Online

ACCESS | Metrics & More | Article Recommendations | SI Supporting Information

ABSTRACT: Theoretical calculation not only is a powerful tool to deeply explore photophysical processes of the emitters but also provides a theoretical basis for material renewal and design strategy in the future. In this work, the interconversion and decay rates of the thermally activated delayed fluorescence (TADF) process of the rigid Ag(dbp)(P$_2$-nCB) complex are quantitatively calculated by employing the optimally tuned range-separated hybrid functional (ω*B97X-D3) method combined with the path integral approach to dynamics considering the Herzberg−Teller and the Duschinsky rotation effects within a multimode harmonic oscillator model. The calculated results show that the small energy splitting $\Delta E(S_1−T_1) = 742$ cm^{-1} (experimental value of 650 cm^{-1}) of the lowest singlet S_1 and triplet T_1 state and proper vibrational spin−orbit coupling interactions facilitate the reverse intersystem crossing (RISC) processes from the T_1 to S_1 states. The k_{RISC} rate is estimated to be 1.72×10^8 s^{-1} that is far more than the intersystem crossing rate k_{ISC} of 7.28×10^7 s^{-1}, which will greatly accelerate the RISC process. In addition, the multiple coupling routes of zero-field splitting (ZFS) interaction can provide energetically nearby lying states, to speed up the RISC pathway, and restrict the phosphorescence decay rate. A smaller ZFS D-tensor of 0.143 cm^{-1}, $E/D \approx 0.094 \ll 1/3$, and $\Delta g > 0$ are obtained, indicating that the excited singlet states are hardly mixed into the T_1 state; thus, a lower phosphorescence decay rate ($k_p = 9.29 \times 10^1$ s^{-1}) is expected to occur, and the T_1 state has a long lifetime, which is helpful for the occurrence of the RISC process. These works are in excellent agreement with the experimental observation and are useful for improving and designing efficient TADF materials.
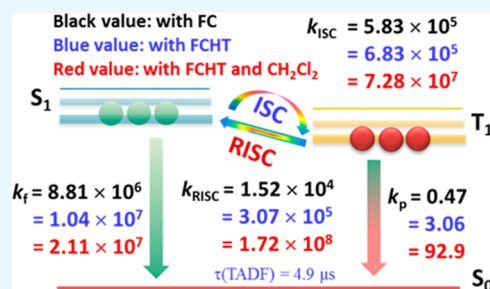
1. INTRODUCTION

Currently, organic light-emitting diodes (OLEDs) are widely used in high-end smartphones, high-resolution TVs, solid-state lighting, and other fields due to their advantages of high contrast, ultrathin nature, flexibility, high efficiency, nontoxic nature, and so on, and the market scale is still further expanding.[1−4] The key to the rapid improvement of OLED performance is the upgradation of luminescent materials. However, the exciton is produced in the ratio of the singlet state to the triplet of 1:3 according to the spin-statistical quantum mechanism during the charge recombination processes; thus, the internal quantum efficiency (IQE) of the triplet exciton for the transition forbidden radiation decay is limited to 75% (see Figure 1).[4] Therefore, how to realize 100% IQE by efficiently harvesting triplet excitons has become a hot issue and difficult topic in the OLED field in recent 30 years, and searching for a new generation of OLED materials has become the main focus of scientists' research.[5−7]

Recent studies have found that some compounds, such as low-cost and environmentally friendly Cu(I) complexes, as well as with purely organic molecules,[5−8] display thermally activated delayed fluorescence (TADF) in OLEDs and can harvest all excitons and achieve nearly 100% IQE (Figure 1).

Consequently, the TADF molecule as a candidate material of the third-generation OLEDs has also attracted much attention. In TADF emitters, a fast reverse intersystem crossing (RISC) process from a triplet (T_1) to a singlet manifold (S_1) with the help of thermal energy at room temperature is the key to the efficient utilization of triplet excitons.[4,9]

However, RISC is a spin-forbidden process, and the spin-flipping rate as the necessary condition to harvest the nonradiative T_1 state into radiative S_1 in TADF molecules is generally low, which greatly limits its application in OLEDs.[10,11] Many researchers are devoted to resolving this thorny issue.[10−12] We know that the spin-flipping process is traditionally described by the mixing of the singlet and triplet wave functions, and the mixing degree (γ) of these states can be expressed as the relationship $\gamma \propto SOC(S_1−T_1)/\Delta E(S_1\_T_1)$, where $SOC(S_1−T_1)$ is the spin−orbit coupling (SOC) value
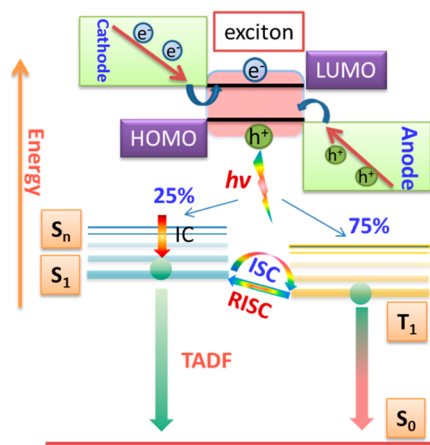
Figure 1. Graphical illustration of the singlet harvesting mechanism based on the TADF pathway after electron−hole recombination in OLEDs.

between the S_1 and T_1 states and $\Delta E(S_1-T_1)$ is their energy gap. According to this relationship, the small $\Delta E(S_1-T_1)$ and large $SOC(S_1-T_1)$ values are requirements for achieving efficient RISC.

From the principles of theoretical chemistry, it is relatively easy to obtain molecules with small $\Delta E(S_1-T_1)$ by structuring a strong charge-transfer (CT) exciton character for the S_1 and T_1 states with the help of a covalently linked electron donor−acceptor (D−A)-type unit. Over the past decade, TADF molecules with small $\Delta E(S_1-T_1)$ values (<0.1 eV) have been reported in a broad series of simple D−A-type molecules;[6,7] in this case, the occurrence of TADF is closely related to the CT S_1 and T_1 states with the frontier orbitals, namely, the highest occupied and lowest unoccupied molecular orbitals (HOMO and LUMO), that are spatially well separated. This leads to an extremely small electron−exchange interaction [equal to $\Delta E(S_1-T_1)/2$; it is a competitive mechanism to suppress ISC through the process of spin conservation] due to small spatial overlap between the HOMO and LUMO.[5] Until now, the design strategy of efficient TADF molecules still mainly focuses on minimizing the gap of $\Delta E(S_1-T_1)$.

It is generally believed that reducing $\Delta E(S_1-T_1)$ is an essential approach to accelerate the conversion from the T_1 to the S_1 state for realizing efficient TADF. Nevertheless, in this understanding, the study of TADF is also confronted with the two dilemmas: one is that some compounds having very small $\Delta E(S_1-T_1)$ represent the poor TADF character and other compounds with a large $\Delta E(S_1-T_1)$ of few hundreds of megaelectron volts have highly efficient TADF, which implies that the $\Delta E(S_1-T_1)$ gap is not the only determining factor for the occurrence of TADF;[13] and the other is that a small $\Delta E(S_1-T_1)$ value with weak exchange interaction between the unpaired electrons requires a small spatial overlap of HOMO and LUMO from the quantum chemical considerations, which results in a weak oscillator strength of the $S_1 \rightarrow S_0$ transition and causes the slow fluorescence rate k_f and low luminescence efficiency. In other words, the corresponding rate k_f and $\Delta E(S_1-T_1)$ are strongly correlated and suppress each other.

Another disadvantage of this strategy in minimizing the $\Delta E(S_1-T_1)$ gap is that the SOC between the S_1 and T_1 states having the same electronic configuration is strictly forbidden because the spin flipping needs to be balanced by the variation of the orbital angular momentum to hold the total momentum

conservation, leading to a negligibly small SOC interaction between the two pure ^{1,3}CT states in the Born−Oppenheimer approximation.[14] This means that the RISC from a CT-type T_1 into a CT-type S_1 is less efficient, no matter how small the $\Delta E(S_1-T_1)$ is, and the calculation results of this paper also support this conclusion, $k_{RISC} \approx 10^4$ s^{-1}. The slow RISC process leads to a long T_1 exciton lifetime and exciton annihilation, which is a vital reason for the serious roll-off effects and material degradation in OLEDs. In 2019, H. Yersin's team[15,16] proposed a new design mechanism for the fourth-generation OLEDs; this design strategy is to provide energetically nearby lying states for the emitting T_1 state to accelerate the RISC process by their SOC and configuration interaction paths. However, it is known that the radiation rate k_P from the T_1 substate to the ground state S_0 is proportional to the relationship $k_P \propto \alpha\Delta E(S_0-T_1)^3|M_j|^2$; here, α is a constant, $\Delta E(S_0-T_1)$ denotes the transition energy, and M_j is the SOC $T_1 \rightarrow S_0$ transition moment and is expressed as follows[17]

$$M_{j \in x,y,z} = \sum_n \frac{\langle S_0|\mu_j|S_n\rangle\langle S_n|\hat{H}_{SOC}|T_1\rangle}{E(T_1) - E(S_n)} + \sum_m \frac{\langle T_1|\mu_j|T_m\rangle\langle T_m|\hat{H}_{SOC}|S_0\rangle}{E(T_m) - E(S_0)} \quad (1)$$

where μ_j represents a projection of the dipole moment operator on the j-axis and $\hat{H}_{SOC}$ is the SOC operator. Based on this relationship, the introduction of strong $\langle S_n|\hat{H}_{SOC}|T_1\rangle$ or $\langle S_n|\hat{H}_{SOC}|T_1\rangle$ interaction paths can not only accelerate the RISC process but also increase the k_P rate. Consequently, it is also a challenge to achieve a rational balance between a strong SOC interaction among nearby low-energy excited states and the k_P rate in designing new TADF molecules.

Based on the above description, in the face of these contradictions and challenges, Yersin and co-workers have experimentally designed and synthesized a Ag(I)-based TADF complex with Ag(dbp)(P$_2$-nCB)[dbp = 2,9-di-n-butyl-1,10-phenanthroline and P$_2$-nCB = $nido$-carborane-bis-(diphenylphosphine)][18,19] with the help of theoretical ideas of high-transition-rate k_f, small $\Delta E(S_1-T_1)$, and structural rigidity to decrease the nonradiative relaxation rate of the excited state (structure shown in Figure 2). It is shown that Ag(dbp)(P$_2$-nCB) displays a 100% emission quantum yield
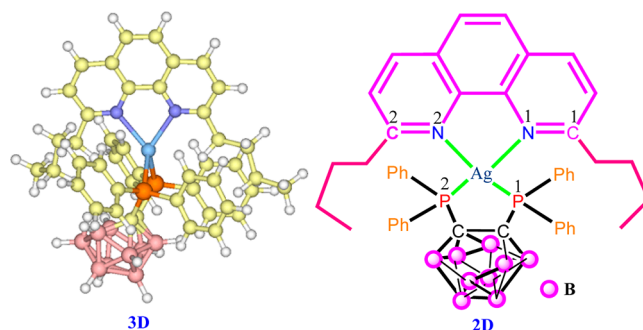

Figure 2. Two- and three-dimensional (2D and 3D) chemical structure with the perspective drawing of the Ag(dbp)(P2-nCB)[dbp = 2,9-di-n-butyl-1,10-phenanthroline and P2-nCB = $nido$-carborane-bis(diphenylphosphine)] complex.

and ultrashort radiation TADF decay time, which is evidently shorter than that of any other TADF materials reported so far.

In contrast to the experimental investigation, the theoretical exploration of the design strategy for the Ag-based TADF complex seems to be extremely backward. However, as an indispensable tool to reveal the nature of the experiment, accurate theoretical calculation can not only provide a quantitative understanding of the photophysical process of the TADF molecule but also possibly trace back to the origin of the experimental results. As mentioned earlier, to provide a new strategy for designing TADF materials, it is essential to fully understand the three correlated processes of two radiations ($S_1 \rightarrow S_0$ and $T_1 \rightarrow S_0$) and one nonradiation of $T_1 \rightarrow S_1$. In the current article, we first quantitatively calculated the emission rates and spectra for the Ag(dbp)(P$_2$-nCB) complex by employing the Fermi golden rule combination of time-dependent density functional theory (TD-DFT) and the path integral approach to dynamics,[20] in which they account for temperature effects, vibronic coupling, and the Duschinsky rotation between modes. Here, the vibronic SOC effects are also considered to calculate the RISC rate relative to the normal-mode coordinate, which is similar to the classical Herzberg−Teller (HT) effect of the dipole transition. Moreover, the contributions of the zero-order Frank−Condon (FC) approximation and the first-order HT effect to radiative rates and spectra are also quantitatively analyzed separately. On the basis of these quantitative analyses, we will refine the theoretical ideas of TADF molecular design in order to provide theoretical supports and new ideas for new design concepts in the future.

2. COMPUTATIONAL DETAILS

Geometry and Electronic Structure Calculations. The version of the ORCA 4.2.1 program package[21] was used to perform all calculations. Geometry optimizations were carried out by employing the BP86 functional together with the resolution of the identity (RI) approximation.[22,23] The BP86 functional was chosen because it provides excellent optimized geometries and a typical accuracy of the vibrational frequencies containing metal complexes. All atoms were first described by the def2-SVP basis set in conjunction with the def2/J and the def2-SVP/C auxiliary basis sets required for the RI approximation.[24] The Becke−Johnson (BJ) damping parameters were also used in Grimme's D3 dispersion correction, writing D3BJ.[25,26] Then, the effective core potential (ECP) of def2-ECP was considered to be recalculated for the metal Ag.[27] In the optimization, we set tight convergence criteria (TightSCF and TightOPT) and increased the integration grids (Grid5 and GridX5), and all the other parameters were chosen as default, unless otherwise specified. Numerical frequency calculations were computed using the same functional and basis set to verify the optimized structures to be the local minima on the potential energy surface. The geometry coordinates are shown in Table S1 of the Supporting Information. The optimized ground-state geometry is found to be well consistent with the experimental X-ray geometry (Tables S2 and S3).[18]

In the calculation of excited-state properties, the traditional DFT may fail completely to predict the properties of the CT excited-state system, which is due to the improper exchange correction approximation and the incorrect behavior at asymptotically large distances.[28] Among the DFT functions, the range-separated hybrid functional is the most satisfactory

method to describe the CT states and has become a tool of choice to study the excited states of such TADF materials when the range-separation parameter is optimally tuned.[29] Therefore, the ωB97X-D3 functional is used to deal with the excited-state properties in the text, and in addition, it is supplemented by the most popular hybrid functional B3LYP calculation. The range-separation parameter ω value is strongly dependent on the studied systems, and ω was tuned by minimizing the target expression 2[29]

$$J^2 = \sum_{i=0}^{1} [\varepsilon_H(N+i) + IP(N+i)]^2 \tag{2}$$

where IP and ε_H indicate the vertical first ionization potential and the HOMO energy of the molecule, respectively. The optimal tuning of ω was performed by using the tuning optDFTw procedure[30] and expressed as ω*B97X-D3.

In the Ag(dbp)(P$_2$-nCB) complex, relativistic effects should be expected, and the scalar relativistic effects were treated by the second-order Douglas−Kroll−Hess (DKH2) method.[31] Electronic vertical absorption and emission were thus simulated using the ω*B97X-D3 and B3LYP functionals in conjunction with the large scalar relativistically recontracted DKH-def2-TZVP(-f) basis set (old-DKH-TZVP for the Ag atom) and the matching auxiliary basis set of SARC/J.[24,32] The RIJCOSX algorithm is also used to accelerate the calculation of the Coulomb and Hartree−Fock exchange integrals in these hybrid functionals.[33] Solvation effects were taken into account by employing the conductor-like polarizable continuum model (CPCM), and toluene ($\varepsilon = 9.08$) was selected as the solvent,[34] which is consistent with the experiment. In this case, the optimal ω* value in the ω*B97X-D3 is calculated to be 0.0102 Bohr^{-1}. The SOC effects along with the Zeeman interactions are obtained from TD-B3LYP or TD-ω*B97X-D3 using the quasi-degenerate perturbation theory (QDPT) approach,[35] where an accurate multicenter spin−orbit mean-field (SOMF) method of the Breit−Pauli SOC operator[36] at all centers leads to a mixing of different multiplicities ($\Delta S = 0, \pm 1$).

Excited-State Dynamics and Spectral Calculation. The dynamic characteristics of excited states, such as fluorescence and phosphorescence rates corresponding to the spectra between an initial state i and a final state f, are obtained by using Fermi's golden rule[37] from quantum electrodynamics combined with the path integration approach (a more detailed description is given in ref 20), which can be expressed as follows[20,38]

$$k(\omega) = \frac{2\omega^3}{3\pi c^3 Z} \sum_{if} e^{-\frac{\varepsilon_i}{k_B T}} \langle \Theta_i | \mu | \Theta_f \rangle \langle \Theta_f | \mu | \Theta_i \rangle \int e^{i(E_i - E_f - \omega)t} dt \tag{3}$$

where μ is the dipole operator, $|\Theta_{i,f}\rangle$ is the vibrational wavefunction of the initial i or final f state, and ε_i is the total vibrational energy; $e^{-\frac{\varepsilon_i}{k_B T}}/Z$ indicates the Boltzmann population at temperature T, and Z is the partition function written as

$$Z = \sum_{i} e^{-\frac{\varepsilon_i}{k_B T}} \tag{4}$$

here, the electronic part of the transition dipole that varies with nuclear displacements is taken into account for emission rates and spectra, and the matrix elements of μ relative to the nuclear coordinates Q_i can be expanded as
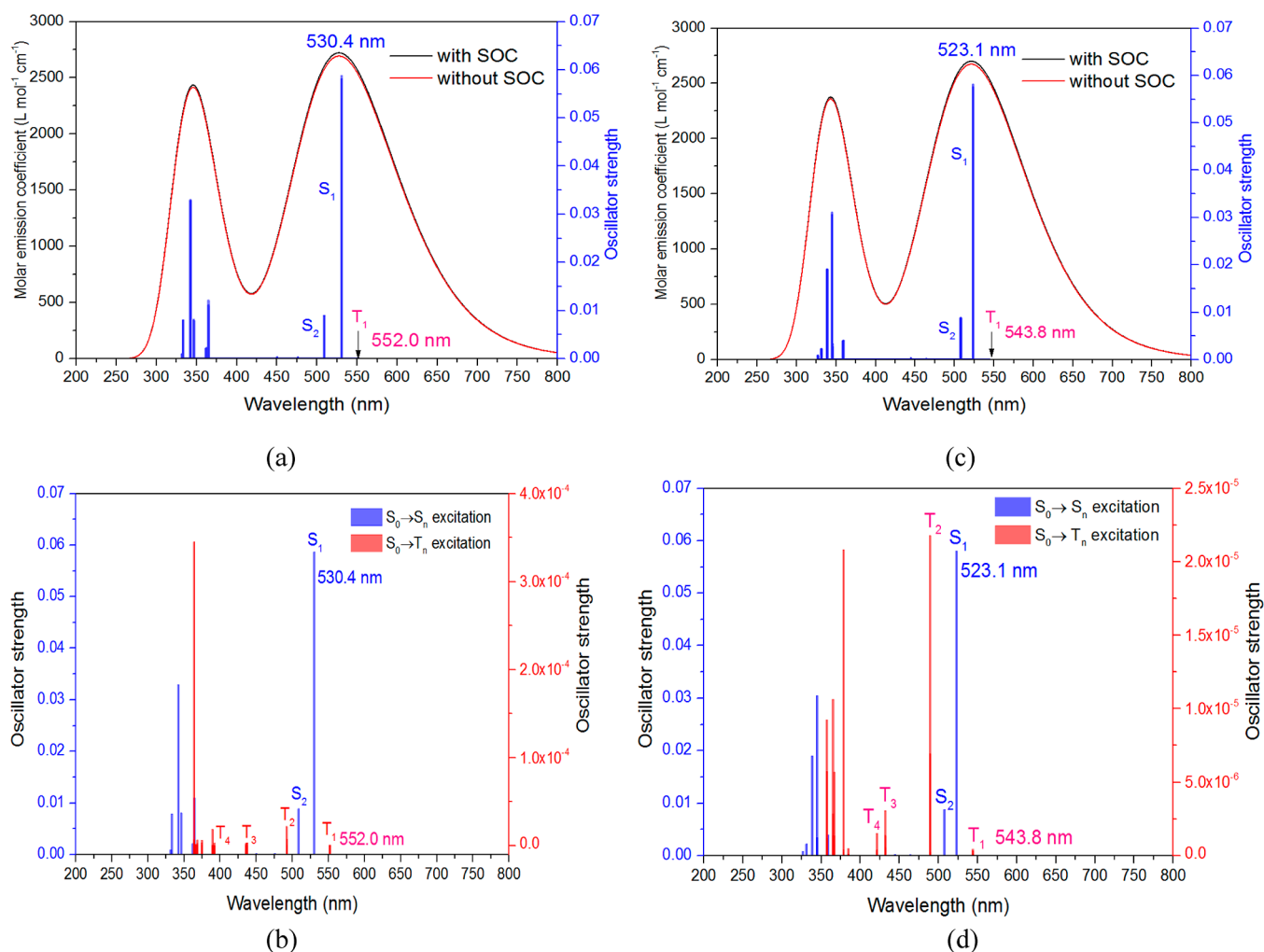
Figure 3. Drawing UV−vis spectra including SOC correction for the liquid CH_2Cl_2 phase at the TD-B3LYP (a,b) and TD-ω*B97X-D3 (c,d) levels, taking into account the DKH2 Hamiltonian scalar relativistic calculation combined with the corresponding recontracted DKH-def2-TZVP(-f) basis set (old-DKH-TZVP for Ag).

$$\mu(Q) = \mu_0 + \sum_i \left.\frac{\partial \mu}{\partial Q_i}\right|_{Q=0} Q_i + \cdots \tag{5}$$

In formula 5, the zero-order term is the FC approximation by keeping only the coordinate independence, and for the second term, only the first-order contribution is considered in the vibration coupling or the so-called HT effect. Note that the expanded transition dipole always chooses the nuclear coordinates of the final state, and all spectra were normalized to one.

The intersystem crossing rates from a given initial state i to a final state f can be also calculated by Fermi's golden rule,[37] which means that the vibrational and electronic contributions to the ISC and RISC rates can be separated. The dependence of temperature, which is particularly critical for the RISC rates, is introduced through a Boltzmann population of the vibrational $\Theta_{i,v}$ level in the i state. In such a case, the ISC rate may be expressed as

$$k_{ISC} = \frac{2\pi}{\hbar Z} \sum_{if} e^{-\frac{\varepsilon_i}{k_B T}} |\langle \Phi_i, \Theta_{i,\nu} | \hat{H}_{SOC} | \Phi_f, \Theta_{f,\nu} \rangle|^2 \delta(E_i - E_f) \tag{6}$$

here, $\hbar$ is the reduced Planck constant, $|\Phi_{i,f}\rangle$ is the orbital wavefunction of the i or f state, and other parameters have the same physical meaning as in eq 3.

As for the coupling contribution of vibration, it is necessary to integrate the electronic and nuclear degrees of freedom. In order to obtain this coupling matrix element in eq 6, it is expanded into a Taylor expansion in the normal coordinates Q_i around the final state as a reference configuration $Q_0 = 0$, see eq 7[39]

$$\langle \Phi_{i,} \Theta_{i,v} | \hat{H}_{SOC} | \Phi_f, \Theta_{f,v} \rangle$$

$$= \langle \Phi_i | \hat{H}_{SOC} | \Phi_f \rangle |_{Q_0=0} \langle \Theta_{i,v} | \Theta_{f,v} \rangle + i \left(\frac{\partial}{\partial Q_i} \langle \Phi_i | \hat{H}_{SOC} | \Phi_f \rangle \right.$$

$$\left. |_{Q_0=0} \langle \Theta_{i,v} | Q_i | \Theta_{f,v} \rangle \right) + \cdots \tag{7}$$

where the first term on the right side is the so-called FC approximation which ignores the dependence of coupling matrix elements on molecular vibration and also named as the direct SOC term; the second term is very similar to the regular HT processing of the elements of the electronic dipole transition matrix, with significant changes in the ISC rates, and

the first-order derivative of this coupling with respect to the normal-mode coordinate is called vibronic SOC.

These calculations were carried out using the new ESD module of the ORCA program recently developed,[21] with default settings and Duschinsky mixing.[40] Moreover, for the sake of speeding up the numerical calculation of the transition dipole moment derivatives, computation is avoided using central differences (labeled CentralDiff = False in ORCA) in all displacements.[20]

3. RESULTS AND DISCUSSION

Electronic Structure of the Excited States. *Spectral Analysis.* The visible spectra of Ag(dbp)(P$_2$-nCB) were simulated by the TD-ω*B97X-D3 and TD-B3LYP methods including SOC correction and using the DKH2 Hamiltonian combined with the corresponding recontracted DKH-def2-TZVP(-f) basis set in CH$_2$Cl$_2$ solution. The band structure and vertical excitation energies, with corresponding oscillator strengths (f), were obtained at each of the vertical excitation to singlet and triplet excited states in TD-DFT calculations, as shown in Figure 3 and Table 1, respectively. In this case, SOC inclusions have no significant effect on the shape of the spectral lines and produce two almost coinciding spectral lines. The obvious difference can be found in any S$_0$ → T$_n$ transition line spectrum, in which the weak oscillator strengths are obtained

Table 1. Selected Low-Energy Vertical Transitions (ΔE in eV) with the Corresponding Oscillator Strengths (f), Natural Transition Orbitals, and Character Assignments for Ag(dbp)(P$_2$-nCB) in the S$_0$ Optimized Geometry at the B3LYP (and ω*B97X-D3)/DKH-def2-TZVP(-f) Theory Level[a]

state	ΔE	f	main contribution[b]	character
			B3LYP	
T$_1$	2.246	5.28×10^{-7}	H ≥ L (94.4%)	^{3}CT
S$_1$	2.338	5.87×10^{-2}	H ≥ L (99.3%)	^{1}CT
S$_2$	2.438	8.87×10^{-3}	H ≥ L+1(98.9%)	^{1}CT
T$_2$	2.518	2.17×10^{-5}	H ≥ L+1 (54.5%), H-3 ≥ L+1 (29.7%)	^{3}CT
S$_3$	2.606	2.14×10^{-4}	H-1 ≥ L (99.0%)	^{1}CT
T$_3$	2.846	3.30×10^{-6}	H ≥ L+1 (42.9%), H-3 ≥ L+1 (32.7%), H-7 ≥ L (6.3%)	^{3}CT
T$_4$	3.163	2.32×10^{-6}	H-3 ≥ L (74.9%), H-2 ≥ L (5.8%), H ≥ L+2 (5.3%)	^{3}CT
T$_5$	3.185	3.13×10^{-6}	H ≥ L+2 (47.3%), H ≥ L+3 (11.6%), H-3 ≥ L (7.8%)	^{3}CT
			ω*B97X-D3	
T$_1$	2.280	4.41×10^{-7}	H ≥ L (95.9%)	^{3}CT
S$_1$	2.370	5.80×10^{-2}	H ≥ L (99.3%)	^{1}CT
S$_2$	2.442	8.77×10^{-3}	H ≥ L+1 (99.0%)	^{1}CT
T$_2$	2.535	2.17×10^{-5}	H ≥ L+1 (66.1%), H-3 ≥ L+1 (23.7%)	^{3}CT
S$_3$	2.672	1.57×10^{-4}	H-1 ≥ L (98.7%)	^{1}CT
T$_3$	2.942	3.06×10^{-6}	H-3 ≥ L+1 (43.2%), H ≥ L+1 (32.2%), H-7 ≥ L (5.8%)	^{3}CT
T$_4$	3.223	1.52×10^{-6}	H-3 ≥ L (85.9%)	^{3}CT
T$_5$	3.274	4.79×10^{-6}	H ≥ L+2 (52.3%), H ≥ L+4 (10.7%), H ≥ L+3 (9.8%)	^{3}CT

[a]CT = charge-transfer state. [b]The highest occupied orbital and the lowest unoccupied orbital are abbreviated as H and L. For example, H-1 is then accordingly the orbital below the HOMO; the percentage in brackets indicates the contribution of the corresponding orbital transition.

due to the singlet−triplet SOC interaction by borrowing the intensity from the coupled singlet−singlet state (see equation 1), such as the S$_0$ → T$_1$ transition, $f = 5.28 \times 10^{-7}$ and 4.41×10^{-7}, and excitation energies of 552.0 and 543.8 nm at the TD-B3LYP and TD-ω*B97X-D3 levels, respectively, indicating that the $\langle S_n | \hat{H}_{SOC} | T_1 \rangle$ interaction is extremely weak. In Figure 3, the spectrum shows the S$_0$ → S$_1$ transition of the stronger spin-allowed band with the maxima at 530.4 (TD-B3LYP) and 523.1 nm (TD-ω*B97X-D3), which is found to be in good agreement with the experimental result of 585 nm in dichloromethane (526 nm for powder), and this also shows that the calculation method is relatively reliable. Besides, the calculated energy splitting of $\Delta E(S_1−T_1)$, from the difference in the vertical excitation energies, is equal to 725 cm^{-1} at the TD-ω*B97X-D3/DKH-def2-TZVP(-f) level, which is thus seen to perfectly match the experimental $\Delta E(S_1−T_1) = 650$ cm^{-1}.[18]

Excited-State Analysis. The frontier orbitals, electron density difference, and transition density maps of selected excitation states of Ag(dbp)(P$_2$-nCB) are shown in Figure 4;
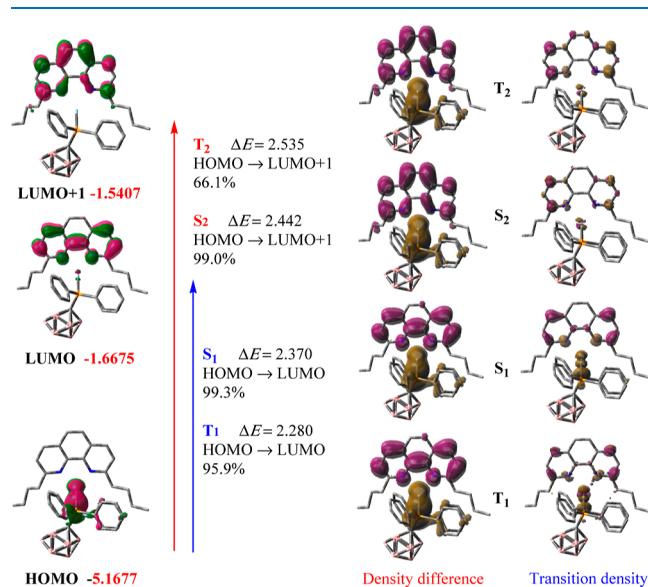

Figure 4. Frontier orbitals (HOMO, LUMO, and LUMO + 1), with the orbital energy in eV, excitation energy ΔE (in eV), transition density difference, and transition density of Ag(dbp)(P2-nCB) for T$_1$, S$_1$, S$_2$, and T$_2$ states calculated at the TD-ω*B97X-D3/DKH-def2-TZVP(-f)(ω* = 0.0102) levels including the scalar relativistic DKH2 Hamiltonian calculation in solution.

see more details in Figures S1−S4 in the Supporting Information. Calculations reveal that the lowest electronic transitions, corresponding to the states S$_1$ and T$_1$ and involving a $\pi \to \pi$* transition from the HOMO to the LUMO, are dominated by single HOMO → LUMO excitation, and the weight values of the TD-ω*B97X-D3 method amount to 99.3 and 95.5%, respectively (Table 1). It can be seen in the orbitals in Figure 4 that the HOMO is located on the metal Ag and phosphorus atoms (go in for silver bonding), while the LUMO represents a π* orbital that spreads over the dbp ligand. This means that the electron density is transferred from the silver and phosphorus atoms to the phenanthroline core of the dbp ligand. The S$_0$ → S$_1$ excitation for the d^9-electronic configuration results in the flattening distortion of the excited S$_1$ states (see Table S2), but the rigid molecular structure of
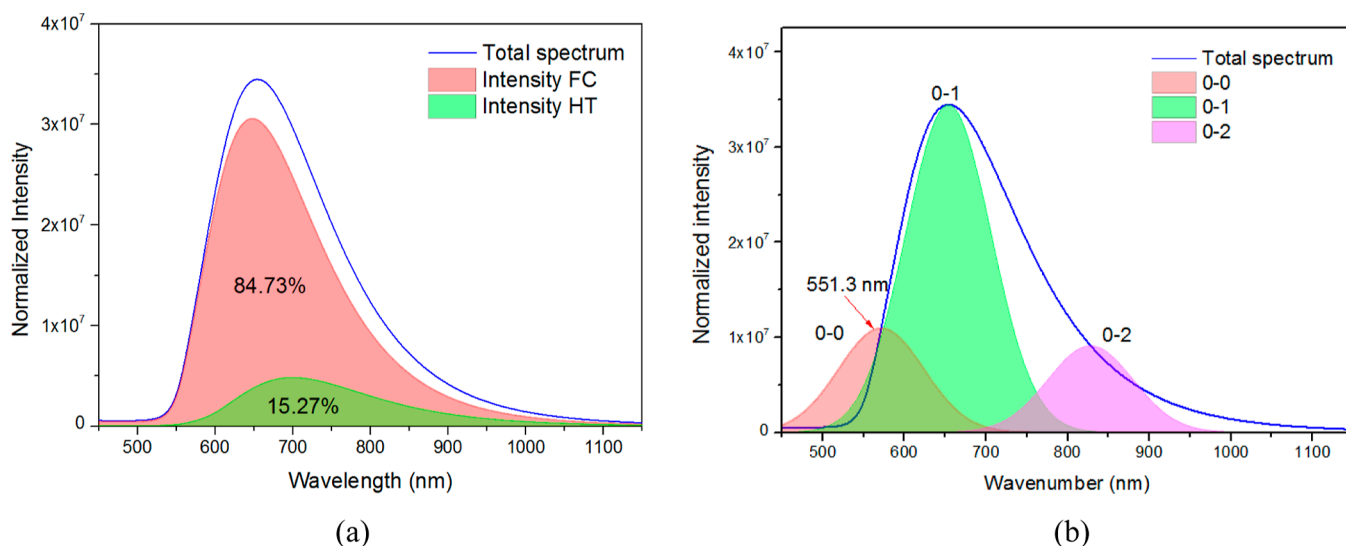
Figure 5. Simulated fluorescence spectra of Ag(dbp)(P$_2$-nCB) at T = 300 K at the B3LYP/def2-TZVP(-f)//def2/J level for dichloromethane. (a) shows the contribution of the FCHT and FC effects and (b) shows the vibrational resolution spectrum.

Ag(dbp)(P$_2$-nCB) restrained this flattening distortion within the reasonable error of ORCA_ESD module calculation.[21] We know that the electron density difference shows the depletion and accumulation of electron density in the process of electron transition, and the coffee color indicates the region of increased electron density in the excited state, whereas purplish-red regions are those of reduced electron density, see Figure 4, and the significant transition density difference is further found between the electron donors of the silver and phosphorus atoms and the acceptor of the dbp ligand; thus, the HOMO and LUMO in Ag(dbp)(P$_2$-nCB) are completely separated, and this HOMO → LUMO excitation is defined to have a typical metal-to-ligand CT characteristic; S$_1$ and T$_1$ are expressed as ^{1,3}CT. Furthermore, the larger electron−electron distance will lead to a larger self-interaction error of the conventional exchange−correlation functional to predict the electronic properties, especially the prediction of excitation energy. Here, the "optimal tuning" ω*B97X-D3 (ω = 0.0102 Bohr^{-1}) functional was selected to describe the electronic structure of the excited state.

The calculations further reveal that the S$_2$ and T$_2$ states come mainly from the HOMO → LUMO + 1 (99.0%) and HOMO → LUMO + 1 (66.1%), respectively, as well as HOMO − 3 → LUMO + 1 (23.7%) transitions, and the S$_3$ state comes from the HOMO − 1 → LUMO (98.7%) transition (Table 1 and Figure 4). Because S$_2$ and T$_1$ (and as S$_1$) have the same type of metal 4d characters in the HOMO and S$_3$ mainly has the characters of CT between the ligands with almost no contributions from the Ag atom, the SOC interactions of these singlet states to the T$_1$ state are expected to be small, which is supported by the spectral calculation including the SOC interactions.

Interestingly, although the S$_1$ state comes from the HOMO → LUMO CT, the oscillator strength of the S$_0$ → S$_1$ transition is predicted to be relatively high; f = 0.0587 (TD-B3LYP) and 0.0580 (TD-ω*B97X-D3). It is commonly known that oscillator strength f is proportional to μ_{HL}^2, called the transition dipole moment for the electron transition, and μ_{HL} can be simplified to[5]

$$\mu_{HL} = e \int \Phi_{HOMO}(r) \vec{r} \Phi_{LUMO}(r) d_r^3 = e \int \rho_{HL}(r) d_r^3 \quad (8)$$

$$\rho_{HL}(r) = \Phi_{HOMO}(r)\Phi_{LUMO}(r) \quad (9)$$

where ρ_{HL} denotes the transition density for the S$_1$ state. From the above equation, the μ_{HL} increases with the increase of the ρ_{HL} value, namely, when ρ_{HL} is distributed in the regions that are far away from the coordinate origin. The calculated transition density is outlined in detail in Figure 4; ρ_{HL} is distributed on the silver and phosphorus atoms and extends over the dbp ligand core that is distant from the origin of the coordinates for the S$_1$ state, leading to a relatively larger μ_{HL} and a larger f, which are beneficial to the fluorescence decay.

On the contrary, the stronger fluorescence may not be conducive to the occurrence of TADF. We know that a key requisite for the TADF occurrence is very small $\Delta E(S_1-T_1)$ with the help of thermal energy, while $\Delta E(S_1-T_1)$ is well approximated by the exchange integral with the HOMO (Φ_{HOMO}) and LUMO (Φ_{LUMO}) for the S$_1$ and T$_1$ states, and it can also be estimated by the transition density ρ_{HL} from the HOMO to LUMO.[5] A smaller $\Delta E(S_1-T_1)$ necessarily requires a smaller transition density ρ_{HL}, which can be described visually by the overlapping integral (S_{HL}) of the HOMO and LUMO, see eq 10, and S_{HL} should have a larger distribution at the intersection of the HOMO and LUMO (see Figure 4).

$$S_{HL}(r) = \int |\Phi_{HOMO}(r)||\Phi_{LUMO}(r)| d_r \quad (10)$$

In this work, the relatively larger f = 0.0587 (TD-B3LYP) of the S$_0$ → S$_1$ transition (or μ_{HL}) appropriately matches with the smaller $\Delta E(S_1-T_1)$ = 725 cm^{-1}, leading to the successful occurrence of TADF.

Fluorescence and Vibronic Coupling. The simulated vibrational fluorescence spectra of Ag(dbp)(P$_2$-nCB) at T = 300 K, taking into account the HT contribution, are depicted in Figure 5, and it can be clearly found that the rigidity of Ag(dbp)(P$_2$-nCB) prevents the distortion of the molecule, where the mode mixing is small, the HT correction only accounts for 15.27% so that the FC approximation is suitable for the study of the fluorescence spectrum. However, the inclusion HT contribution satisfactorily reproduced the overall

Table 2. Simulated FCHT and FC Fluorescence (k_f in s^{-1}) and Phosphorescent (k_p in s^{-1}) Rates of Ag(dbp)(P$_2$-nCB) in Different Environments; Comparison with Published Experimental Data

| | vacuum | | | | solution CH$_2$Cl$_2$ | | | |
| | only FC | | with FCHT[a] | | only FC | | with FCHT | |
temp. (K)	k_f	k_p	k_f	k_p	k_f	k_p	k_f	k_p
77	9.31×10^6	5.20×10^{-1}	1.08×10^7	2.47×10^0	1.89×10^7	1.06×10^0	2.19×10^7	8.31×10^1
			14.31%[b]	96.78%			14.31%	91.64%
300	8.81×10^6	4.66×10^{-1}	1.04×10^7	3.06×10^0	1.79×10^7	6.21×10^0	2.11×10^7	9.29×10^1
			15.27%	97.66%			15.27%	93.21%
exp. data[c]							5.6×10^7 (300 K)	6.7×10^2 (77 K)

[a]FC approximation and incorporation of the HT effect. [b]x % denotes the contribution of HT to the rate. [c]Ref 18.
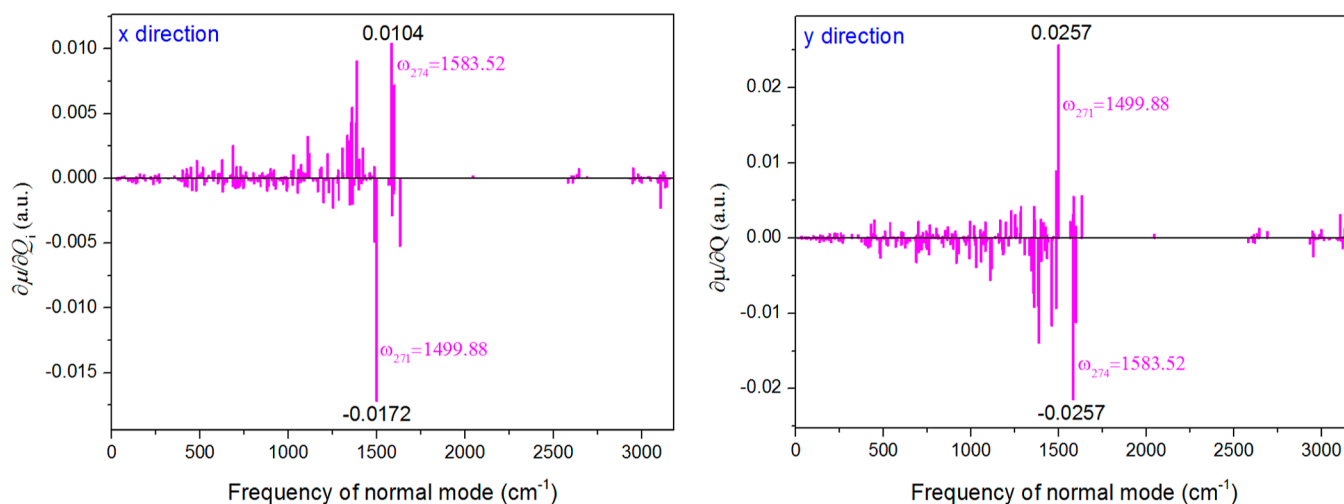

Figure 6. Calculated transition dipole derivatives, $\partial\mu/\partial Q_i$, relative to the normal mode Q_i for the lowest singlet excited state S$_1$ of Ag(dbp)(P$_2$-nCB)(the z direction is not listed).

trend of the band shape, while the peak band position is less accurate, and a red shift of about 50 nm compared with the experimental value of 585 nm in dichloromethane is observed. In the same way, compared to the FC calculation ($k_f = 1.79 \times 10^7$ s^{-1}), inclusion of the HT effect can enhance the decay rate of fluorescence k_f by about 15.27% at $T = 300$ K and $k_f = 2.11 \times 10^7$ s^{-1} (see Table 2), perfectly matching the experimental value of $k_f = 5.6 \times 10^7$ s^{-1}.[18] At a low temperature of 77 K, this HT effect is reduced to 14.31%.

In order to deeply understand the details of the HT effect, eq 5 can be further extended as follows[41]

$$\mu(Q) = \mu_0 \prod_a \langle m_a| + \sum_i \left.\frac{\partial\mu}{\partial Q_i}\right|_{Q=0} \langle m_a|Q_i|n_a\rangle \prod_{a \neq b} \langle m_b|$$
$$+ \cdots \qquad (11)$$

herein, $\partial\mu/\partial Q_i$ is the first derivative of the transition dipole moment with respect to the nuclear coordinate of the normal mode Q_i; $\langle m_a|Q_i|n_a\rangle$ indicates the vibration transition dipole moment; m_a and n_a are the vibration quantum numbers; $\langle m_b|n_b\rangle$ is the overlap integral using the expression of Q_i. The obtained $\partial\mu/\partial Q_i$ and $\langle m_a|Q_i|n_a\rangle$ are depicted in Figures 6 and 7 and Table S4. As seen in Figure 6, the normal modes with $\omega_{271} = 1499.88$ cm^{-1} and $\omega_{274} = 1583.52$ cm^{-1} make remarkable contributions to $\partial\mu/\partial Q_i$ along all three directions (the z direction is not plotted). The two modes mainly originate from the asymmetric stretchings of the C−C and C−P bonds and bending vibrations of ∠C−C−H on the dbp ring. These
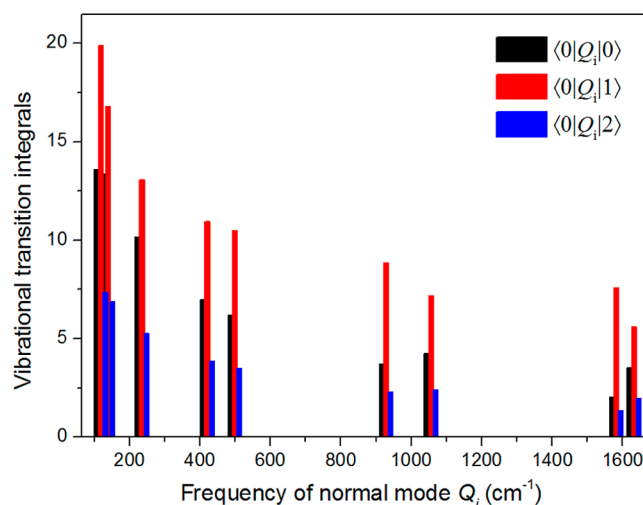

Figure 7. Calculated vibrational transition dipole moment, $\langle 0|Q_i|0\rangle$, $\langle 0|Q_i|1\rangle$, and $\langle 0|Q_i|2\rangle$ with respect to the normal mode Q_i for the fluorescence emission of Ag(dbp)(P$_2$-nCB).

vibration modes may produce the most intense 0−1 lines at 631.7 nm, which are in perfect agreement with the fluorescence data. The contribution from the normal modes of 1300 to 1650 cm^{-1} would have a slight influence on the line shape of the fluorescence spectrum.

In addition, the FC emission intensity (the first term in equation 11) is proportional to the FC factor and can be evaluated as[42]

$$\mathrm{FC}_{S_{0,n_a},S_{1,0}} = \frac{S_a^{n_a}}{n_a!}e^{-S_a} \qquad (12)$$

where S_a represents the Huang−Rhys factor, which can reflect the vibronic coupling strength. On the basis of eq 12, the FC factor is directly proportional to the Huang−Rhys factor with $n_a > 0$ when the S_a is lower than 1.0. The peak intensity is directly decided by the S_a factor, but the strongest FC strength should be the position of $n_a = 0$. As can be seen in Figure 8, all
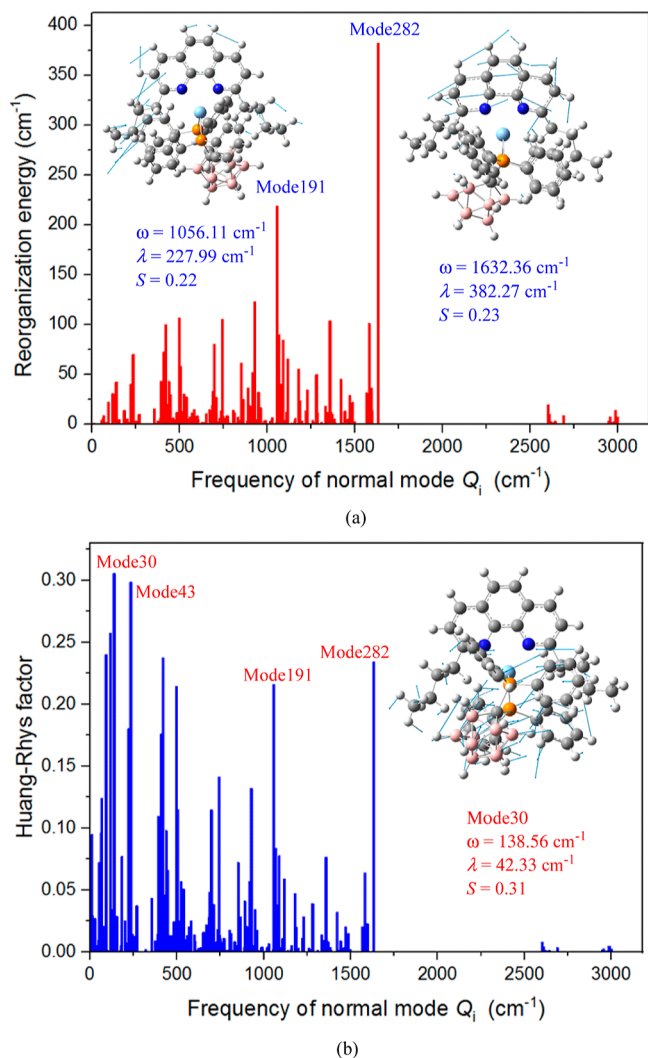

(a)

(b)

Figure 8. Calculated reorganization energies (a) and Huang−Rhys factors (b) vs the normal-mode frequencies during the $S_1 \rightarrow S_0$ process; vibration modes of the largest reorganization energy were inserted into the picture for the S_1 state.

S_a factors for the normal modes are smaller than 1.0, suggesting the central emission corresponding to the 0−0 transition. However, the spectral band would be broadened for Ag(dbp)-(P$_2$-nCB) with the bigger total Huang−Rhys factors, especially when the temperature increases (see Figure 5). At the same time, the maximum peak value in Figure 5 is red-shifted in comparison with the highest peak in Figure 3 owing to the inhomogeneous broadening effect. The low-frequency normal

modes, such as ω_{30}, ω_{43}, and so forth, have larger S_a factors, indicating the larger displacement; simultaneously, the $\partial\mu/\partial Q_i$ derivations are very small, which provides a weak vibronic line intensity (Figure 6). The high-frequency normal modes (~1500 cm^{-1}) are the main contributions to the low-energy emission peaks and have larger reorganization energies, showing the extent of vibronic coupling between the two electronic states, see Figure 8, $\omega_{191} = 1056.11$ cm^{-1}, $S_{191} = 0.22$ and $\omega_{282} = 1632.36$ cm^{-1}, $S_{282} = 0.23$. These vibrations come from the stretchings of the C−C and C−P bonds on the ring of the dbp ligand. To put it in another way, the Huang−Rhys factor is derived from the natural frequency difference of the two structures, and the material has thus sufficient fluorescence stability.

Spin Mixing and Reverse Intersystem Crossing. It is generally accepted that reducing $\Delta E(S_1−T_1)$ is an essential approach to promote RISC from the T_1 to S_1 state for an efficient TADF. However, the opposite examples of efficient TADF complexes with the larger $\Delta E(S_1−T_1)$ have shown that $\Delta E(S_1−T_1)$ is not the only determining factor of efficient TADF. Indeed, theoretical research reveals that only when there is an internal magnetic interaction such as SOC inducing spin mixing between the singlet and triplet states, the RISC depending on $\Delta E(S_1−T_1)$ can be verified to generate TADF. Also, the spin-mixing parameter, γ, can be simply written as $\gamma^2 = \xi^2/\Delta^2$,[43] which is the sum of the orbital mixing and spin mixing; herein, ξ is the SOC strength and Δ is the energy difference between the two states. Besides, the ratio between the spin-flip rate to the spin-conserving one is estimated by $\chi^2 = 4/3\gamma^2$, and all calculated values along the optimized T_1 step (see Figure S5) are shown in Table 3 and Figure 9. In calculations, we observe that Ag(dbp)(P$_2$-nCB) was found to have a very small spin-mixing γ^2 and spin-flip rate χ^2, lying within a range of ~10^{-5} and ~10^{-6}, respectively. As stated above, the γ^2 is proportional to the SOC strength ξ^2, while the direct SOC between the S_1 and T_1 states is totally forbidden, that is, $\langle{}^1\mathrm{CT}(S_1)|H_{\mathrm{SOC}}|^3\mathrm{CT}(T_1)\rangle$ falls to zero (Figure 9, detailed data seen in Tables S5 and S6 of the Supporting Information), leading to a small χ^2. Even if the SOC effect of the T_2 state increases slightly, the energy difference increases sharply, which also gives rise to the small spin-mixing and spin-flip rate. On the spin admixture, no large variation is observed along the optimized T_1 step in the RISC process, which shows that the orbital configurations have not changed greatly.

Our calculated k_{ISC} and k_{RISC} rate constants are given in Table 4, including the HT and Duschinsky mixing effects. As seen in Table 4, interestingly, the k_{RISC} mainly increased by 2 orders of magnitude, while the k_{ISC} hardly changed when the temperature increased from 77 to 300 K. That is to say, the rate of k_{RISC} is more susceptible to temperature than that of k_{ISC}, and it is mainly attributed to the failure to satisfy the conservation of energy with $\Delta E(S_1−T_1) < 0$. At 300 K, the k_{RISC} constant of $T_1 \rightarrow S_1$ is estimated to be 1.72×10^8 s^{-1}, which is far more than the ISC rate k_{ISC} of 7.28×10^7 s^{-1} in CH$_2$Cl$_2$ solution. Meanwhile, the phosphorescence k_p rate value is expected to be very small as 9.29×10^1 s^{-1} owing to the smaller SOC and larger energy difference. In such a situation, the k_{RISC} is more favorable to compete with these rates at room temperature, therefore the S_1 state can be repopulated from the T_1 state by the RISC pathway, and delayed fluorescence possibly occurs.

What is more, we also noted that the vibrational SOC interaction (HT effect) makes a great contribution to k_{RISC} at

Table 3. Calculated Spin Admixture Parameter (γ^2) and Spin-Flip (χ^2) along the Optimized T$_1$ Step from the S$_1$ Geometry

optimization steps	γ^2(S$_1$-T$_1$)	γ^2(S$_1$-T$_2$)	χ^2(S$_1$-T$_1$)	χ^2(S$_1$-T$_2$)
		B3LYP		
1st	2.35×10^{-5}	1.02×10^{-6}	3.13×10^{-5}	1.36×10^{-6}
5th	2.28×10^{-5}	1.08×10^{-6}	3.05×10^{-5}	1.44×10^{-6}
13th	2.26×10^{-5}	1.08×10^{-6}	3.01×10^{-5}	1.44×10^{-6}
19th	2.11×10^{-5}	1.06×10^{-6}	2.81×10^{-5}	1.43×10^{-6}
24th	2.01×10^{-5}	1.05×10^{-6}	2.67×10^{-5}	1.39×10^{-6}
28th	2.05×10^{-5}	1.04×10^{-6}	2.73×10^{-5}	1.38×10^{-6}
33rd	2.13×10^{-5}	1.03×10^{-6}	2.84×10^{-5}	1.38×10^{-6}
		ω*B97X-D3		
1st	4.13×10^{-5}	1.11×10^{-6}	5.51×10^{-5}	1.48×10^{-6}
5th	4.48×10^{-5}	1.17×10^{-6}	5.97×10^{-5}	1.56×10^{-6}
13th	4.52×10^{-5}	1.18×10^{-6}	6.03×10^{-5}	1.57×10^{-6}
19th	4.19×10^{-5}	1.18×10^{-6}	5.58×10^{-5}	1.57×10^{-6}
24th	4.14×10^{-5}	1.15×10^{-6}	5.52×10^{-5}	1.54×10^{-6}
28th	4.24×10^{-5}	1.14×10^{-6}	5.65×10^{-5}	1.52×10^{-6}
33rd	4.19×10^{-5}	1.14×10^{-6}	5.59×10^{-5}	1.52×10^{-6}
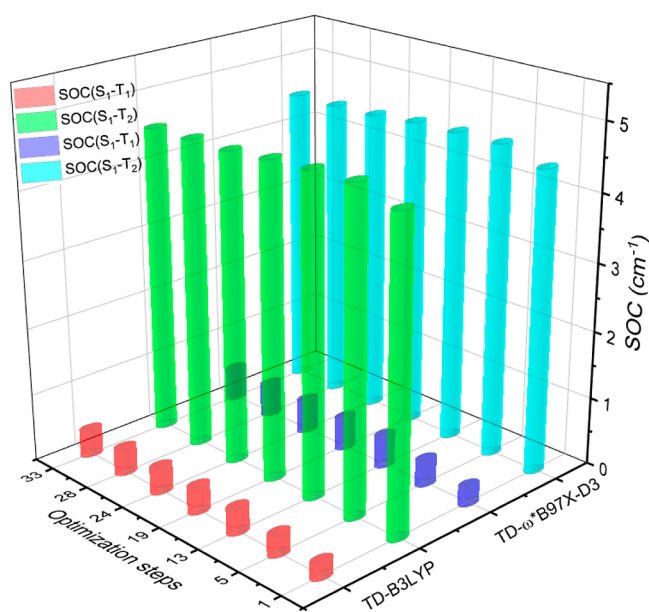
Figure 9. Calculated spin−orbital coupling matrix elements between the S$_1$ and T$_{1,2}$ states in the T$_1$ structure for Ag(dbp)(P$_2$-nCB) at the TD-B3LYP and TD-ω*B97X-D3/DKH-def2-TZVP(-f)//SARC/J levels.

300 K, accounting for 89.88% of the total rate while only 65.55% for the k_{ISC} in solution, which further indicates that the HT effect plays a vital role in improving RISC conversion. To deeply explore the vibrational SOC effect, we calculated the relationship between $\langle S_1|H_{SOC}|T_1\rangle$ and Q_i, as shown in Figure 10. The involvement of the normal modes with low-frequency vibrations (<1600 cm^{-1}) can be quantitatively observed by calculating the derivatives of these individual modes, leading to a tremendous increase of the SOC interaction. The average value (red line) of $\partial\langle S_1|H_{SOC}|T_1\rangle/\partial Q_i$ for the RISC T$_1 \rightarrow$ S$_1$ process is 1 order of magnitude higher than that of $\partial\langle S_1|H_{SOC}|T_1\rangle/\partial Q_i$ (black) for the ISC process in the CH$_2$Cl$_2$ solution. These results indicate that the S$_1$ state may be directly populated and lead to delayed fluorescence in solution.

Phosphorescence and Zero-Field Splitting. As eq 1 described above, the phosphorescence rate k_p is proportional to the spin−orbit-coupled T$_1 \rightarrow$ S$_0$ transition moment M_j in the case of the invariant ΔE(T$_1$−S$_0$) gap. Thus, the higher-lying states have to be considered because they can mix into the emitting triplet state via direct or indirect SOC, which divides the T$_1$ manifold into three energy-separated sublevels in the absence of an external field. This splitting is called as zero-field splitting, and it is normally measured as the D-tensor.[44] Furthermore, the spin and orbital angular momenta interact with an external magnetic field, leading to the Zeeman interaction characterized by the g-factor, which can be used as a measure of the effective SOC. The distinction between the

Table 4. Calculated Intersystem Crossing (k_{ISC}, for S$_1 \rightarrow$ T$_1$) and Reverse Intersystem Crossing (k_{RISC}, for T$_1 \rightarrow$ S$_1$) Rates Taking into Account the HT Effect of Ag(dbp)(P$_2$-nCB); All Units in s^{-1}; $k_{ISC}{}^0$ for the T$_1 \rightarrow$ S$_0$ Crossing Rate

	vacuum only FC			solution CH$_2$Cl$_2$ only FC		
temp.(K)	k_{ISC}	k_{RISC}	$k_{ISC}{}^0$	k_{ISC}	k_{RISC}	$k_{ISC}{}^0$
77	7.63×10^5	4.67×10^4	9.50×10^4	6.26×10^7	6.90×10^6	1.93×10^5
300	5.83×10^5	1.52×10^4	1.51×10^5	4.78×10^7	2.24×10^6	3.06×10^5
	with FCHT[a]			with FCHT		
temp. (K)	k_{ISC}	k_{RISC}		k_{ISC}	k_{RISC}	
77	1.38×10^5	1.54×10^4		1.29×10^7	6.28×10^6	
	13.42%[b]	5.28%		24.17%	73.59%	
300	6.83×10^5	3.07×10^5		7.28×10^7	1.72×10^8	
	55.23%	61.74%		65.55%	89.88%	

[a]FC approximation and incorporating the HT effect. [b]x % denotes the contribution of HT to the rate.
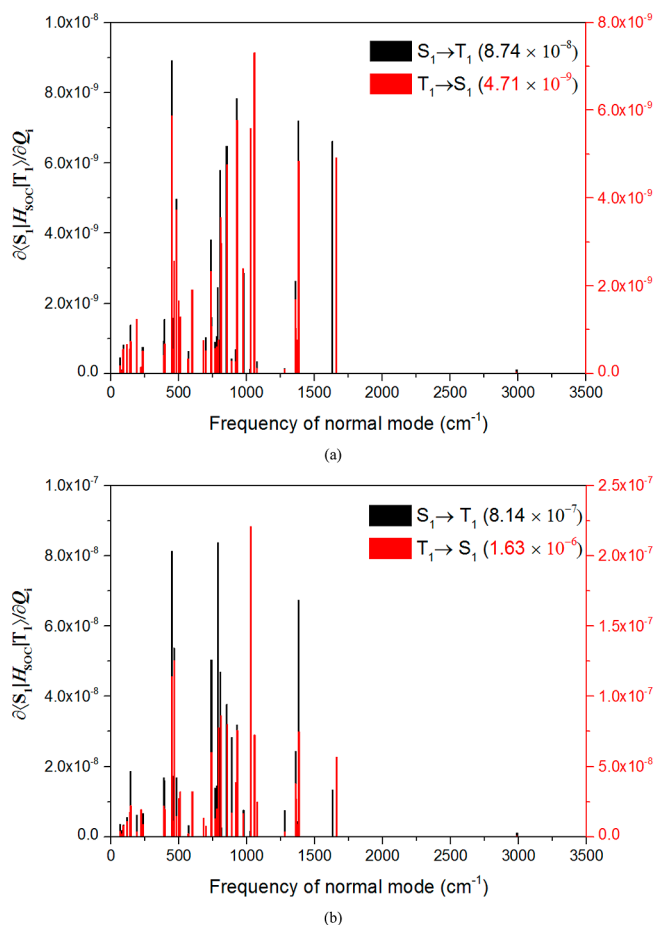
(a)

(b)

Figure 10. First derivatives of SOC with respect to normal-mode coordinate Q_i between S_1 and T_1 based on the HT effect: (a) gas phase and (b) CH_2Cl_2. The data in parentheses represents the total value of the first derivatives of SOC.

Figure 11. Diagram from the vital excitation analysis of the contributions to the individual components of Δg_{iso} and $D(\alpha \rightarrow \beta)$ of the T_1 state for the $Ag(dbp)(P_2\text{-}n\text{CB})$ compound.

shown, the D parameters are very small, that is, 0.13719 and 0.14265 cm^{-1} at the B3LYP and ω^*B97X-D3 levels, respectively; the E/D value is smaller and far less than 1/3, which means that the excited states are hardly mixed into the T_1 state. In order to further explore the contribution origins of the D-tensor, the SOC contribution is decomposed into different types of excitations. It is found that the larger contribution of SOC to the D-tensor mainly comes from the excitations of spin-allowed $T_1 \rightarrow T_m$ transitions. The spin-pairing (i.e., triplet $\rightarrow$ singlet) excitations are minimal, accounting for about 0.04% of the D-tensor at the ω^*B97X-D3 level, which implies that the excited singlet states can hardly be mixed into the T_1 state by the SOC interactions, leading to a smaller $T_1 \rightarrow S_0$ transition moment M_j, as expected, and it is helpful for the occurrence of the RISC process.

The g-shift (Δg), as a measure for effective SOC, is also given in Table 5 and Figure 11. According to the formulation proposed by F. Neese, Δg can be decomposed as follows[46]

$$g = g_e + \Delta g = g_e + \Delta g^{RMC} + \Delta g^{DSO} + \Delta g^{PSO} \quad (13)$$

where g_e is equal to 2.0023193, Δg^{RMC} denotes a relativistic mass correction, Δg^{DSO} is a diamagnetic spin−orbit correction, and Δg^{PSO} is the orbital Zeeman and SOC cross-term, termed $\Delta g^{OZ/SOC}$. It can be seen in Table 5 that Δg virtually depends on the third term, Δg^{PSO}, while Δg^{RMC}, like other relativistic effects, is negligibly small in $Ag(dbp)(P_2\text{-}n\text{CB})$. The second

two tensors (D-tensor and g-factor) is that only the excited states with the same total spin as the T_1 state contribute to the g-factor, whereas the D-tensor contains terms not only from the same spin excited states but also from different spin excited states.[45]

The calculated parameters of the g-factor and D-tensor using the ω^*B97X-D3/B3LYP methods and the individual contributions are exhibited in Table 5, and some vital excitation analysis of the contributions can be seen in Figure 11. As
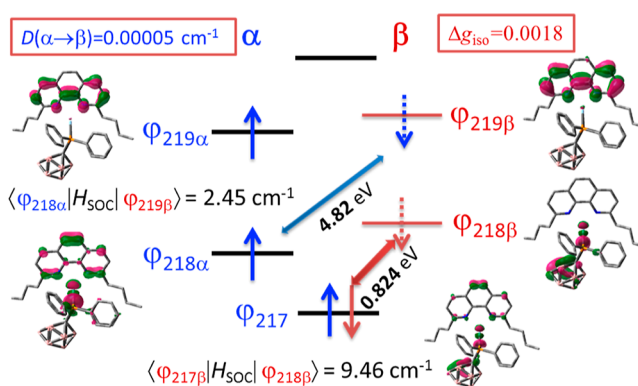
Table 5. Calculated Zero-Field Splitting Tensors (D and E in Cm^{-1}) and g-Factor Constants of the Triplet-State T_1 Using the Quasi-Restricted Orbital (QRO) Approach in the CPCM (CH_2Cl_2) for $Ag(dbp)(P_2\text{-}n\text{CB})$

method	contributions		D	E		g_x	g_y	g_z
B3LYP	SOC	$\alpha \rightarrow \alpha$	0.06431	0.00450	g^{RMC}	−0.0001812	−0.0001812	−0.0001812
		$\beta \rightarrow \beta$	0.04216	0.02089	g^{DSO}	0.0004367	0.0003999	0.0005068
		$\alpha \rightarrow \beta$	0.00005	0.00005	g^{PSO}	0.0002673	0.0015798	0.0027703
		$\beta \rightarrow \alpha$	0.03066	−0.00986	$g(tot)^a$	2.0028421	2.0041178	2.0054152
		total	0.13719	0.01559	Δg^b	0.0005228	0.0017985	0.0030960
ω^*B97X-D3	SOC	$\alpha \rightarrow \alpha$	0.06769	0.00135	g^{RMC}	−0.0001830	−0.0001830	−0.0001830
		$\beta \rightarrow \beta$	0.04105	0.01760	g^{DSO}	0.0004334	0.0004058	0.0005083
		$\alpha \rightarrow \beta$	0.00006	0.00006	g^{PSO}	0.0002794	0.0015817	0.0027993
		$\beta \rightarrow \alpha$	0.03386	−0.00568	$g(tot)^a$	2.0028491	2.0041239	2.0054440
		total	0.14265	0.01334	Δg^b	0.0005298	0.0018046	0.0031247

$^a g_{iso} = 1/3(g_x + g_y + g_z)$ and $g_e = 2.0023193$. $^b \Delta g_{iso} = 1/3(\Delta g_x + \Delta g_y + \Delta g_z)$.

term Δg^{DSO} is also relatively small and has an opposite sign for the Δg^{RMC} term, nearly canceling.

We know that Δg^{PSO} originates from the interaction of the SOC and external magnetic field, and only transitions between the orbital coupling pairs, with a small energy gap and a large SOC interaction, can contribute efficiently to Δg^{PSO}. Also, the coupling of the different spin space (α and β electron) actually leads to different negative and positive contributions to the Δg^{PSO} tensor. As shown in Figure 11, the effective coupling involving the vacant β spinor, $\langle\varphi_{217\beta}|H_{SOC}|\varphi_{218\beta}\rangle = 9.46$ cm^{-1}, and $\Delta E(\varphi_{217\beta}-\varphi_{218\beta}) = 0.824$ eV produces positive Δg, $g > 2.0023193$ (see Table 5), that is to say, leading to the deshielding contributions.[46] This indicates that the interaction between metal Ag and the dbp ligand is a weak bond, and this electronic structure inhibits the SOC between different spin states, which makes it possible for TADF to occur.

4. CONCLUSIONS

To date, the design strategy of efficient TADF molecules is still mainly focused on minimizing the gap of $\Delta E(S_1-T_1)$. However, we all know that the $\Delta E(S_1-T_1)$ gap is not the only determining factor for the occurrence of TADF. Thus, it became a challenge to design and develop efficient TADF materials.

Theoretical calculation is an indispensable and powerful method for the investigation and design of new materials. The main purpose of this article is to quantitatively calculate the photophysical parameters of the three key processes of TADF occurrence for the rigid Ag(dbp)(P$_2$-nCB) complex by means of an accurate quantum calculation method combined with the path integral approach to dynamics, which accounts for temperature effects, vibronic coupling, and the Duschinsky rotation between modes. Based on these quantitative analyses, we obtain the results as follows: (i) first, regulating the relationship between the transition dipole moment μ_{HL} of $S_0 \rightarrow S_1$ and the energy gap $\Delta E(S_1-T_1)$ of the excited singlet S_1 and triplet T_1 states because the μ_{HL} and $\Delta E(S_1-T_1)$ are approximately proportional to the transition density ρ_{HL} from the HOMO to LUMO, while they are inversely proportional to each other for efficient TADF. In text, the relatively larger $f = 0.0587$ (TD-B3LYP) of the $S_0 \rightarrow S_1$ transition (or μ_{HL}) appropriately matches with the smaller $\Delta E(S_1-T_1) = 725$ cm^{-1}, and a relatively small $\Delta E(S_1-T_1)$ is required −for efficient TADF materials, leading to the successful occurrence of TADF; (ii) second, regulating the relative sizes of the spin−orbit admixtures between the T_1 state and excited singlets, a smaller ZFS D-tensor of 0.143 cm^{-1}, $E/D \approx 0.094 \ll 1/3$, and $\Delta g > 0$ are all obtained, indicating that the excited singlet states are hardly mixed into the T_1 state; thus, a lower phosphorescence decay rate (k_p) is expected to occur, which is helpful for the occurrence of the RISC process. In vacuum, $k_{RISC} = 4.67 \times 10^4$ s$^{-1} \gg k_p = 5.20 \times 10^{-1}$ s^{-1} for the FC approximation at 77 K; (iii) third, the HT, temperature, and environmental effects must be considered in the nonradiative ISC process, especially k_{RISC}. The calculated results show that the vibrational SOC interaction (HT effect) makes a great contribution to k_{RISC} at 300 K, accounting for 89.88% of the total rate in solution, and the k_{RISC} mainly increases by 2 orders of magnitude, while k_{ISC} hardly changes when the temperature rises from 77 to 300 K, and the k_{RISC} is estimated to be 1.72×10^8 s^{-1}, which is far more than the ISC rate k_{ISC} of 7.28×10^7 s^{-1} in CH$_2$Cl$_2$ solution; (iv) the rigid structure together with the strongly electron-donating negatively charged P$_2$-nCB

ligand for Ag(dbp)(P$_2$-nCB) is also one of the design principles.

■ ASSOCIATED CONTENT

Ⓢ Supporting Information

The Supporting Information is available free of charge at https://pubs.acs.org/doi/10.1021/acsomega.2c00036.

> Coordinates of the optimized geometric structure for Ag(dbp)(P$_2$-nCB); comparison of selected geometry parameters of Ag(dbp)(P$_2$-nCB); frontier orbitals, excitation energy ΔE (in eV), transition density difference and transition density for T$_1$, S$_1$, S$_2$, and T$_2$ states at the TD-B3LYP/DKH-def2-TZVP(-f) level; vital vibrational frequency (ω_i in cm^{-1}), reorganization energy (λ_i in cm^{-1}), Huang−Rhys factor (S_i), and vibrational transition dipole moment integral for the lowest singlet excited state S$_1$; SOC matrix elements between T$_m$ and S$_n$ states; and energy change diagrams of the optimized S$_1$ step from the T$_1$ geometry (PDF)

■ AUTHOR INFORMATION

Corresponding Author

LingLing Lv − *School of Chemical Engineering and Technology, Tianshui Normal University, Tianshui, Gansu 741001, China; Supercomputing Center for Theoretical Chemistry, Tianshui Normal University, Tianshui, GanSu 741001, China;* ⓞ orcid.org/0000-0001-6208-6629; Email: lvling002@163.com, lvling100@163.com

Authors

Kun Yuan − *School of Chemical Engineering and Technology, Tianshui Normal University, Tianshui, Gansu 741001, China; Supercomputing Center for Theoretical Chemistry, Tianshui Normal University, Tianshui, GanSu 741001, China*

TianYu Zhao − *School of Chemical Engineering and Technology, Tianshui Normal University, Tianshui, Gansu 741001, China; Supercomputing Center for Theoretical Chemistry, Tianshui Normal University, Tianshui, GanSu 741001, China*

HuiXue Li − *School of Chemical Engineering and Technology, Tianshui Normal University, Tianshui, Gansu 741001, China; Supercomputing Center for Theoretical Chemistry, Tianshui Normal University, Tianshui, GanSu 741001, China*

YongCheng Wang − *College of Chemistry and Chemical Engineering, Northwest Normal University, Lanzhou, Gansu 730070, China*

Complete contact information is available at: https://pubs.acs.org/10.1021/acsomega.2c00036

Notes

The authors declare no competing financial interest.

■ ACKNOWLEDGMENTS

■ REFERENCES

(1) Yang, Z.; Mao, Z.; Xie, Z.; Zhang, Y.; Liu, S.; Zhao, J.; Xu, J.; Chi, Z.; Aldred, M. P. Recent advances in organic thermally activated delayed fluorescence materials. *Chem. Soc. Rev.* **2017**, *46*, 915−1016.

(2) Tao, Y.; Yuan, K.; Chen, T.; Xu, P.; Li, H.; Chen, R.; Zheng, C.; Zhang, L.; Huang, W. Thermally Activated Delayed Fluorescence Materials Towards the Breakthrough of Organoelectronics. *Adv. Mater.* **2014**, *26*, 7931−7958.

(3) *Highly Efficient OLEDs Materials Based on Thermally Activated Delayed Fluorescence*; Yersin, H., Ed.; Wiley-VCH: Weinheim, Germany, 2019.

(4) Uoyama, H.; Goushi, K.; Shizu, K.; Nomura, H.; Adachi, C. Highly efficient organic light-emitting diodes from delayed fluorescence. *Nature* **2012**, *492*, 234−238.

(5) Czerwieniec, R.; Leitl, M. J.; Homeier, H. H. H.; Yersin, H. Cu(I) complexes − Thermally activated delayed fluorescence. Photophysical approach and material design. *Coord. Chem. Rev.* **2016**, *325*, 2−28.

(6) Wong, M. Y.; Zysman-Colman, E. Purely organic thermally activated delayed fluorescence for organic light-emitting diodes. *Adv. Mater.* **2017**, *29*, 1605444.

(7) Liu, Y.; Li, C.; Ren, Z.; Yan, S.; Bryce, M. R. All organic thermally activated delayed fluorescence materials for organic light-emitting diodes. *Nat. Rev. Mater.* **2018**, *3*, 18020.

(8) Lv, L.; Yuan, K.; Si, C.; Zuo, G.; Wang, Y. Mechanism study of TADF and phosphorescence in dinuclear copper (I) molecular crystal using QM/MM combined with an optimally tuned range-separated hybrid functional. *Org. Electron.* **2020**, *81*, 105667−105679.

(9) Noda, H.; Nakanotani, H.; Adachi, C. Excited state engineering for efficient reverse intersystem crossing. *Sci. Adv.* **2018**, *4*, No. eaao6910.

(10) Noda, H.; Chen, X.-K.; Nakanotani, H.; Hosokai, T.; Miyajima, M.; Notsuka, N.; Kashima, Y.; Brédas, J.-L.; Adachi, C. Critical role of intermediate electronic states for spin-flip processes in charge-transfer-type organic molecules with multiple donors and acceptors. *Nat. Mater.* **2019**, *18*, 1084−1090.

(11) Cui, L.-S.; Gillett, A. J.; Zhang, S.-F.; Ye, H.; Liu, Y.; Chen, X.-K.; Lin, Z.-S.; Evans, E. W.; Myers, W. K.; Ronson, T. K.; Nakanotani, H.; Reineke, S.; Brédas, J.-L.; Adachi, C.; Friend, R. H. Spin-flip enables efficient and stable organic electroluminescence from charge-transfer states. *Nat. Photonics* **2020**, *14*, 636−642.

(12) Penfold, T. J.; Gindensperger, E.; Daniel, C.; Marian, C. M. Spin-vibronic mechanism for intersystem crossing. *Chem. Rev.* **2018**, *118*, 6975−7025.

(13) Wang, M.; Chatterjee, T.; Foster, C. J.; Wu, T.; Yi, C.-L.; Yu, H.; Wong, K.-T.; Hu, B. Exploring mechanism of generating spin-orbital coupling through donor-acceptor design to realize spin flipping in thermally activated delayed fluorescence. *J. Mater. Chem. C* **2020**, *8*, 3395−3401.

(14) Rausch, A. F.; Homeier, H. H. H.; Yersin, H. Organometallic Pt(II) and Ir(III) triplet emitters for OLED applications and the role of spin−orbit coupling: A study based on high-resolution optical spectroscopy. *Top. Organomet. Chem.* **2010**, *29*, 193−235.

(15) Yersin, H.; Mataranga-Popa, L.; Czerwieniec, R.; Dovbii, Y. Design of a new mechanism beyond thermally activated delayed fluorescence toward fourth generation organic light emitting diodes. *Chem. Mater.* **2019**, *31*, 6110−6116.

(16) Yersin, H.; Mataranga-Popa, L.; Li, S.-W.; Czerwieniec, R. Design strategies for materials showing thermally activated delayed fluorescence and beyond: Towards the fourth-generation OLED mechanism. *J. Soc. Inf. Disp.* **2018**, *26*, 194−199.

(17) Baryshnikov, G.; Minaev, B.; Ågren, H. Theory and calculation of the phosphorescence phenomenon. *Chem. Rev.* **2017**, *117*, 6500−6537.

(18) Shafikov, M. Z.; Suleymanova, A. F.; Czerwieniec, R.; Yersin, H. Design strategy for Ag(I)-based thermally activated delayed fluorescence reaching an efficiency breakthrough. *Chem. Mater.* **2017**, *29*, 1708−1715.

(19) Shafikov, M. Z.; Suleymanova, A. F.; Czerwieniec, R.; Yersin, H. Thermally activated delayed fluorescence from Ag(I) complexes: A route to 100% quantum yield at unprecedentedly short decay time. *Inorg. Chem.* **2017**, *56*, 13274−13285.

(20) de Souza, B.; Farias, G.; Neese, F.; Izsák, R. Predicting phosphorescence rates of light organic molecules using time-dependent density functional theory and the path integral approach to dynamics. *J. Chem. Theory Comput.* **2019**, *15*, 1896−1904.

(21) Neese, F. Software update: the ORCA program system, version 4.0. *Wiley Interdiscip. Rev.: Comput. Mol. Sci.* **2018**, *8*, No. e1327.

(22) Becke, A. D. Density-functional exchange-energy approximation with correct asymptotic behavior. *Phys. Rev. A* **1988**, *38*, 3098−3100.

(23) Vahtras, O.; Almlöf, J.; Feyereisen, M. W. Integral approximations for LCAO-SCF calculations. *Chem. Phys. Lett.* **1993**, *213*, 514−518.

(24) Weigend, F.; Ahlrichs, R. Balanced basis sets of split valence, triple zeta valence and quadruple zeta valence quality for H to Rn: Design and assessment of accuracy. *Phys. Chem. Chem. Phys.* **2005**, *7*, 3297−3305.

(25) Grimme, S.; Antony, J.; Ehrlich, S.; Krieg, H. A consistent and accurate Ab Initio parametrization of density functional dispersion correction (DFT-D) for the 94 Elements H-Pu. *J. Chem. Phys.* **2010**, *132*, 154104.

(26) Grimme, S.; Ehrlich, S.; Goerigk, L. Effect of the damping function in dispersion corrected density functional theory. *J. Comput. Chem.* **2011**, *32*, 1456−1465.

(27) Andrae, D.; Haussermann, U.; Dolg, M.; Stoll, H.; Preuss, H. Energy-adjusted ab initio pseudo potentials for the second and third row transition elements. *Theor. Chim. Acta* **1990**, *77*, 123−141.

(28) Körzdörfer, T.; Brédas, J. L. Organic electronic materials: recent advances in the DFT description of the ground and excited states using tuned range-separated hybrid functionals. *Acc. Chem. Res.* **2014**, *47*, 3284−3291.

(29) Sun, H.; Zhong, C.; Brédas, J.-L. Reliable prediction with tuned range-separated functionals of the singlet−triplet gap in organic emitters for thermally activated delayed fluorescence. *J. Chem. Theory Comput.* **2015**, *11*, 3851−3858.

(30) Lu, T. *optDFTw and scanDFTw program v1.0.* http://sobereva.com/346 (2017.3.8).

(31) Sandhoefer, B.; Neese, F. One-electron contributions to the g-tensor for second-order Douglas-Kroll-Hess theory. *J. Chem. Phys.* **2012**, *137*, 094102.

(32) Weigend, F. Accurate Coulomb-fitting basis sets for H to Rn. *Phys. Chem. Chem. Phys.* **2006**, *8*, 1057−1065.

(33) Neese, F.; Wennmohs, F.; Hansen, A.; Becker, U. Efficient, approximate and parallel Hartree−Fock and hybrid DFT calculations. A 'chain-of-spheres' algorithm for the Hartree−Fock exchange. *Chem. Phys.* **2009**, *356*, 98−109.

(34) Barone, V.; Cossi, M. Quantum calculation of molecular energies and energy gradients in solution by a Conductor Solvent Model. *J. Phys. Chem. A* **1998**, *102*, 1995−2001.

(35) Roemelt, M.; Maganas, D.; DeBeer, S.; Neese, F. A combined DFT and restricted open-shell configuration interaction method including spin-orbit coupling: Application to transition metal L-edge X-ray absorption spectroscopy. *J. Chem. Phys.* **2013**, *138*, 204101.

(36) Neese, F. Efficient and accurate approximations to the molecular spin-orbit coupling operator and their use in molecular g-tensor calculations. *J. Chem. Phys.* **2005**, *122*, 034107.

(37) Schatz, G. C.; Ratner, M. A. *Quantum Mechanics in Chemistry*, 1st ed.; Dover Publications: Mineola, N.Y, 2002.

(38) de Souza, B.; Neese, F.; Izsák, R. On the theoretical prediction of fluorescence rates from first principles using the path integral approach. *J. Chem. Phys.* **2018**, *148*, 034104.

(39) Daza, M. C.; Doerr, M.; Salzmann, S.; Marian, C. M.; Thiel, W. Photophysics of phenalenone: quantum-mechanical investigation of singlet−triplet intersystem crossing. *Phys. Chem. Chem. Phys.* **2009**, *11*, 1688−1696.

(40) Baiardi, A.; Bloino, J.; Barone, V. General time dependent approach to vibronic spectroscopy including Franck—Condon, Herzberg—Teller, and Duschinsky Effects. *J. Chem. Theory Comput.* **2013**, *9*, 4097—4115.

(41) Minaev, B.; Wang, Y.-H.; Wang, C.-K.; Luo, Y.; Ågren, H. Density functional theory study of vibronic structure of the first absorption Q x band in free-base porphin. *Spectrochim. Acta, Part A* **2006**, *65*, 308—323.

(42) Scholz, R.; Kleine, P.; Lygaitis, R.; Popp, L.; Lenk, S.; Etherington, M. K.; Monkman, A. P.; Reineke, S. Investigation of thermally activated delayed fluorescence from a donor—acceptor compound with time-resolved fluorescence and density functional theory applying an optimally tuned range-separated hybrid functional. *J. Phys. Chem. A* **2020**, *124*, 1535—1553.

(43) Xu, H.; Wang, M.; Yu, Z.-G.; Wang, K.; Hu, B. Magnetic field effects on excited states, charge transport, and electrical polarization in organic semiconductors in spin and orbital regimes. *Adc. Phys.* **2019**, *68*, 49—121.

(44) Neese, F. Importance of direct spin—spin coupling and spin-flip excitations for the zero-field splittings of transition metal complexes:A case study. *J. Am. Chem. Soc.* **2006**, *128*, 10213—10222.

(45) Neese, F. Quantum chemistry and EPR parameters. *eMagRes* **2017**, *6*, 1—22.

(46) Bora, P. L.; Novotný, J.; Ruud, K.; Komorovsky, S.; Marek, R. Electron-spin structure and metal-ligand bonding in open-shell systems from relativistic EPR and NMR: A case study of square-planar iridium catalysts. *J. Chem. Theory Comput.* **2019**, *15*, 201—214.